

**\*\*FULL TITLE\*\***  
*ASP Conference Series, Vol. \*\*VOLUME\*\*, \*\*YEAR OF PUBLICATION\*\**  
**\*\*NAMES OF EDITORS\*\***

## Non-thermal emission from Massive Young Stellar Objects

E. R. Parkin, J. M. Pittard, M. G. Hoare

*School of Physics and Astronomy, The University of Leeds, Woodhouse Lane, Leeds LS2 9JT, UK*

**Abstract.** In the young stellar object (YSO) phase of their lives, massive stars drive bi-polar molecular outflows. These outflows produce beautiful, often hourglass shaped, cavities. The central star possesses a powerful stellar wind ( $v \sim 2000 \text{ kms}^{-1}$ ), and possibly a dense equatorial disk wind ( $v \sim 400 \text{ kms}^{-1}$ ), which collide with the inner surface of the bi-polar cavity and produces hot ( $T \sim 10^5 - 10^8 \text{ K}$ ) shocked plasma. A reverse shock is formed at the point where the ram pressure between the preshock flow balances the thermal pressure of the postshock flow and provides a site for the acceleration of non-thermal particles to relativistic energies. Hydrodynamical models of the wind interaction, coupled with calculations of the non-thermal energy spectrum, are used to explore the observable synchrotron and gamma-ray emission from these objects.

### 1. Introduction

The formation of massive stars involves outflows (Garay & Lizano 1999; Reipurth & Bally 2001; Banerjee & Pudritz 2006, 2007). Bi-polar cavities around YSOs are commonly observed in star formation (Garay & Lizano 1999), with collimation factors of  $\sim 2 - 10$  for massive YSOs (MYSOs) (Beuther et al. 2002; Davis et al. 2004). Numerical simulations of high-mass star formation show that outflows are a by-product of the collapse process which forms the massive star, and may be due to radiation pressure and magnetic fields (Yorke & Sonnhalter 2002; Banerjee & Pudritz 2007). The termination shock of an MYSO jet can provide a site for particle acceleration (Araudo et al. 2007).

The widths of IR recombination line emission observed from MYSOs indicates the presence of dense outflows with velocities ranging from 100 to  $> 340 \text{ kms}^{-1}$  (Drew et al. 1993; Bunn et al. 1995). Further confirmation of outflows has come from high angular resolution radio observations (e.g. Hoare et al. 1994; Hoare 2006). One explanation would be a disk wind generated when UV flux from the star is absorbed and re-emitted by the material at the surface of the disk (e.g. Drew et al. 1998).

X-rays have been detected from deeply embedded MYSOs in star forming regions by the *Chandra X-ray observatory* (hereafter *Chandra*) (e.g. Wang et al. 2007, 2009). An initial observation of Mon R2 detected X-ray emission from the intermediate mass objects consistent with the hard and highly time variable X-ray emission caused by magnetic flaring activity between the star and disk (Kohno et al. 2002). Further analysis of the same data, coupled with high resolution near-IR interferometry identified the separate constituents of Mon R2 IRS3 (Preibisch et al. 2002). The X-ray emission from IRS3 A and C, with a

count rate of  $0.166 \pm 0.041 \text{ ks}^{-1}$  for the former, could not be explained by the standard scenario for massive stars (i.e. wind embedded shocks produced by instabilities inherent in radiatively-driven winds - see Owocki et al. 1988), yet the estimated stellar masses of these objects implies they will have radiative outer envelopes which poses problems for the generation of X-rays through magnetic recombination between the star and disk. In this work we examine another potential source of X-rays, namely the collision between the outflowing stellar and disk winds and the infalling envelope.

We find that the interaction of the stellar and disk wind with the cavity wall produces shock heated plasma which emits X-rays in agreement with *Chandra* observations (Parkin et al. 2009, in prep). The reverse shock, plus weak shocks within the hot gas, provide a site for particle acceleration. Therefore, a timely question, considering the recent launch of the Fermi Gamma-ray Space Telescope (*Fermi*), is whether the winds-cavity interaction produces an observable non-thermal energy spectrum extending up to  $\gamma$ -ray energies. To this aim we have developed our existing model for thermal X-ray emission to consider non-thermal radio and  $\gamma$ -ray emission.

## 2. Winds-cavity interaction

The model consists of a MYSO situated at the centre of a previously evacuated bipolar cavity which is surrounded by infalling molecular cloud material. We include the stellar wind and a disk wind which emanates from the surface of the circumstellar accretion disk; both are assumed to be at terminal velocity. Due to the spatial scales under consideration we do not attempt to model the radiative driving of the winds as this requires high spatial resolution in the vicinity of the star/disk (e.g. Owocki et al. 1994; Proga et al. 1998). For simplicity we adopt an angle dependant wind prescription, whereby the stellar wind occupies a region up to a polar angle of  $60^\circ$  and the disk wind occupies the region from  $60^\circ - 85^\circ$ . The density and velocity distributions for the infalling cloud material are described by the equations of Terebey et al. (1984). The morphology of the pre-existing outflow cavity is described by a simple analytical prescription similar to that of Alvarez et al. (2004).

We consider a  $\sim 30 M_\odot$  O8V star with a mass-loss rate of  $10^{-7} M_\odot \text{ yr}^{-1}$  and terminal wind speed of  $2000 \text{ kms}^{-1}$ . The disk wind has a mass-loss rate of  $10^{-6} M_\odot \text{ yr}^{-1}$  and a terminal wind speed of  $400 \text{ kms}^{-1}$ . The unshocked winds are assumed to be at a temperature of  $10^4 \text{ K}$ . The mass infall rate for the cloud is  $2 \times 10^{-4} M_\odot \text{ yr}^{-1}$  and the cavity opening angle is  $30^\circ$ . The winds-cavity interaction was followed for a simulation time of  $t = 2000 \text{ yrs}$ .

Examining Fig. 1 we see that the disk wind, which has a post-shock temperature of  $\sim 10^6 \text{ K}$ , lines the cavity wall beyond which resides the infalling cloud material. The hotter post-shock stellar wind fills a volume closer to the pole. A reverse shock is established within  $\sim 10^{16} \text{ cm}$  of the star/disk which can be clearly seen in the temperature plot of Fig. 1. The shape and position of the reverse shock fluctuates with time causing variability in the observed emission on timescales of  $\sim 50 \text{ yrs}$ . The shocked stellar and disk winds reach temperatures up to  $\sim 10^8 \text{ K}$  and  $\sim 10^6 \text{ K}$ , respectively.

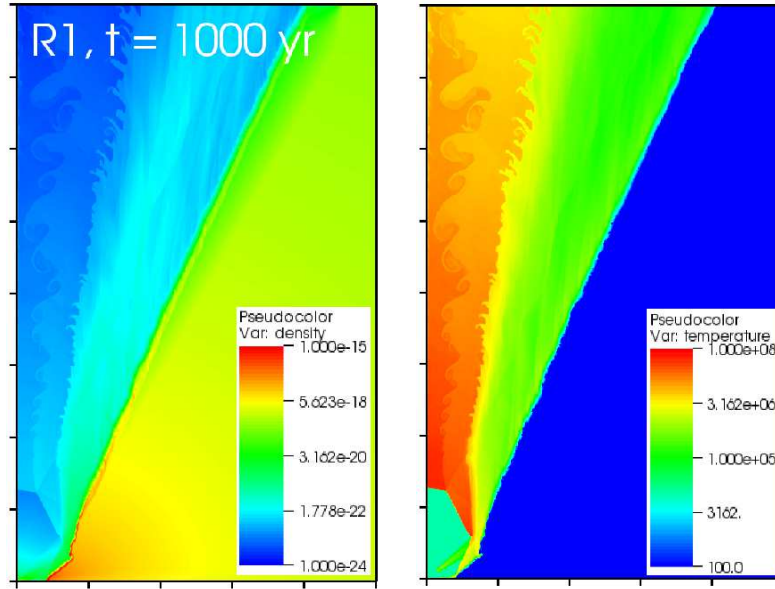


Figure 1. Density (left) and temperature (right) snapshots taken from a hydrodynamic model of the wind-cavity interaction at  $t = 1000$  yrs. The tick marks on the axis correspond to a distance of  $10^{16}$  cm.

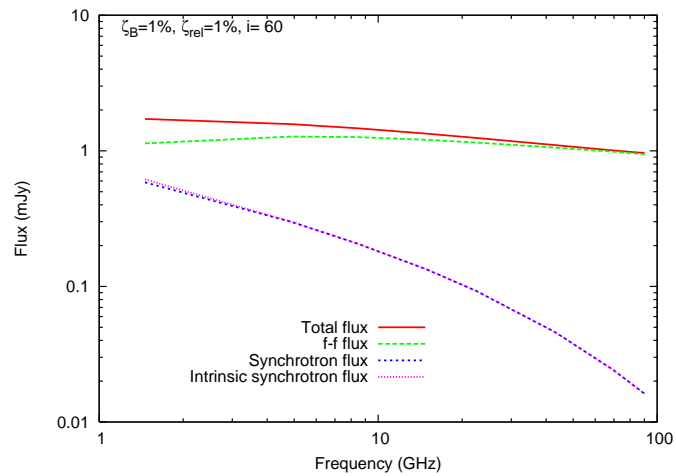


Figure 2. 1-100 GHz radio spectrum calculated from the hydrodynamic simulation shown in Fig. 1 using an inclination angle of  $60^\circ$ . In this plot  $\zeta_B = \zeta_{rel} = 1\%$ .

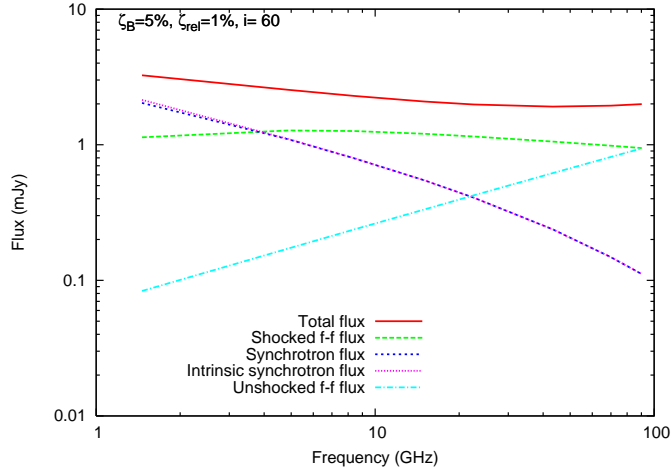


Figure 3. Same as Fig. 2 except  $\zeta_B = 5$ . The contribution to the free-free flux from the unshocked stellar and disk winds and the shocked plasma are shown.

Thermal X-ray emission in agreement with *Chandra* observations of MYSOs (e.g. Kohno et al. 2002; Preibisch et al. 2002; Giardino et al. 2004) is produced by the shocked gas adjacent to the reverse shock. In particular, hard X-rays are produced ( $E > 5$  keV), the simulated ACIS-I count rate is  $\sim 0.2$  ks $^{-1}$ , and the visual extinction to the star is  $\sim 30 - 100$  mag (corresponding to a column of  $5.7 - 190 \times 10^{21}$  cm $^2$ ). We note that the emission weighted column density (Parkin & Pittard 2008), which is indicative of the column density to the regions of highest intrinsic emission, is higher than the column density to the star.

### 3. Radio Emission

The reverse shock present in the simulations provides a site for the acceleration of non-thermal particles to relativistic energies. We calculate the synchrotron emission and absorption, the Razin effect, and Inverse Compton (IC) cooling of electrons. The non-thermal and magnetic field energy densities are assumed to be proportional to the thermal energy density. The non-thermal particle distribution is described by a power-law distribution with  $p = 2$ . The ratio of the magnetic to thermal energy density is  $\zeta_B$ , and similarly the ratio of the relativistic particle to thermal energy density is  $\zeta_{rel}$ . The free-free emission from the ionized winds is also calculated.

Fig. 2 shows the resulting radio spectrum when  $\zeta_B = \zeta_{rel} = 1\%$  is assumed. The total spectrum has a flat slope, indicative of optically thin plasma. The free-free emission from the unshocked winds is lower than the contribution from the shocked winds inside the cavity. The thermal emission is dominant; the synchrotron emission only has a small impact on the total spectrum at low frequencies. Increasing the post-shock magnetic energy density ( $\zeta_B = 5\%$ ) causes a rise in the magnitude of the synchrotron emission (Fig. 3) and alters the slope

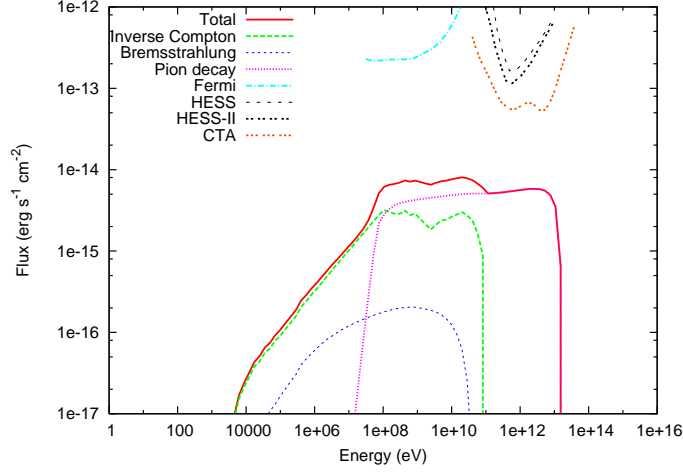


Figure 4. Non-thermal energy spectrum calculated from the hydrodynamic simulation shown in Fig. 1 where  $\zeta_B = \zeta_{\text{rel-e}} = \zeta_{\text{rel-p}} = 5\%$ . The sensitivity curve for the Cherenkov Telescope Array (*CTA*) is from Bernlöhner et al. (2008).

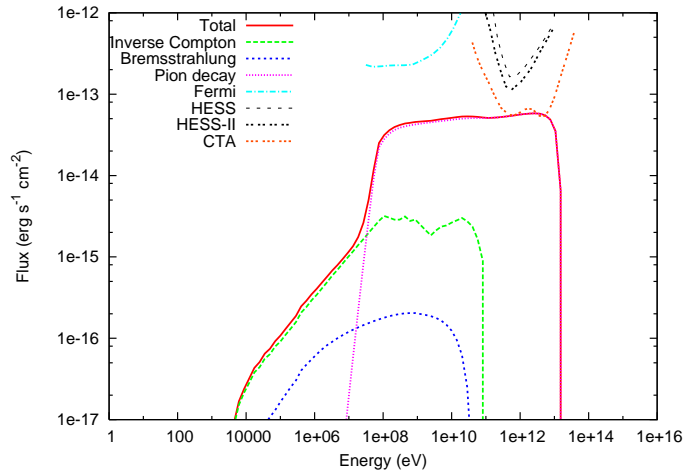


Figure 5. Same as Fig. 4 except  $\zeta_{\text{rel-p}} = 50\%$

of the observed spectrum. With this in mind the observed radio spectrum could be used to constrain parameter values for the magnetic and relativistic particle energy density. However, a major difficulty with this approach lies in attaining observational constraints due to the low surface brightness and large spatial extent of the emission region; typical observations of massive star forming regions strive for high spatial resolution which resolves out emission on the scales we are interested in.

#### 4. Gamma-ray emission

To examine the possibility of observable  $\gamma$ -ray emission we calculate the emission from: Relativistic Bremsstrahlung, IC emission, and Pion decay. Fig. 4 shows that IC emission is dominant at low energies whilst Pion decay is dominant at higher energies. For  $\zeta_B = \zeta_{\text{rel-e}} = \zeta_{\text{rel-p}} = 5\%$  the observed flux is considerably weaker than the sensitivity of *Fermi*, *HESS*, *HESS-II*, and *CTA*. In the case of efficient particle acceleration ( $\zeta_{\text{rel-p}} = 50\%$ ) this gap is reduced and there is a tentative possibility of a detection with *CTA* (Fig. 5). These results then imply that  $\gamma$ -ray emission will not be detectable from a single MYSO.

We close with the note that the possibility of detecting non-thermal  $\gamma$ -ray emission may be increased if consideration is given to the cumulative effects of a cluster of massive stars, or, in the case of efficient particle acceleration, from single MYSOs more massive than our test case O8V star.

**Acknowledgments.** ERP thanks the University of Leeds for funding through a Henry Ellison Scholarship. JMP gratefully acknowledges funding from the Royal Society. We would also like to thank Jim Hinton for useful conversations.

#### References

- Alvarez, C., Hoare, M., & Lucas, P. 2004, *A&A*, 419, 203  
 Araudo, A. T., Romero, G. E., Bosch-Ramon, V., & Paredes, J. M. 2007, *A&A*, 476, 1289  
 Banerjee, R. & Pudritz, R. E. 2006, *ApJ*, 641, 949  
 Banerjee, R. & Pudritz, R. E. 2007, *ApJ*, 660, 479  
 Bernlöhner, K., Carmona, E., & Schweizer, T. 2008, in International Cosmic Ray Conference Vol. 3 of International Cosmic Ray Conference, MC Simulation and Layout Studies for a future Cherenkov Telescope Array. pp 1469–1472  
 Beuther, H., Schilke, P., Gueth, F., McCaughrean, M., Andersen, M., Sridharan, T. K., & Menten, K. M. 2002, *A&A*, 387, 931  
 Bunn, J. C., Hoare, M. G., & Drew, J. E. 1995, *MNRAS*, 272, 346  
 Davis, C. J., Varricatt, W. P., Todd, S. P., & Ramsay Howat, S. K. 2004, *A&A*, 425, 981  
 Drew, J. E., Bunn, J. C., & Hoare, M. G. 1993, *MNRAS*, 265, 12  
 Drew, J. E., Proga, D., & Stone, J. M. 1998, *MNRAS*, 296, L6+  
 Garay, G. & Lizano, S. 1999, *PASP*, 111, 1049  
 Giardino, G., Favata, F., & Micela, G. 2004, *A&A*, 424, 965  
 Hoare, M. G. 2006, *ApJ*, 649, 856  
 Hoare, M. G., Drew, J. E., Muxlow, T. B., & Davis, R. J. 1994, *ApJ*, 421, L51  
 Kohno, M., Koyama, K., & Hamaguchi, K. 2002, *ApJ*, 580, 626  
 Owocki, S. P., Castor, J. I., & Rybicki, G. B. 1988, *ApJ*, 335, 914  
 Owocki, S. P., Cranmer, S. R., & Blondin, J. M. 1994, *ApJ*, 424, 887

- Parkin, E. R. & Pittard, J. M. 2008, MNRAS, 388, 1047  
Preibisch, T., Balega, Y. Y., Schertl, D., & Weigelt, G. 2002, A&A, 392, 945  
Proga, D., Stone, J. M., & Drew, J. E. 1998, MNRAS, 295, 595  
Reipurth, B. & Bally, J. 2001, ARA&A, 39, 403  
Terebey, S., Shu, F. H., & Cassen, P. 1984, ApJ, 286, 529  
Wang, J., Feigelson, E. D., Townsley, L. K., Román-Zúñiga, C. G., Lada, E., & Garmire, G. 2009, ApJ, 696, 47  
Wang, J., Townsley, L. K., Feigelson, E. D., Getman, K. V., Broos, P. S., Garmire, G. P., & Tsujimoto, M. 2007, ApJS, 168, 100  
Yorke, H. W. & Sonnhalter, C. 2002, ApJ, 569, 846